Published in final edited form as:

Laser Photon Rev. 2020 ; 14(9): . doi:10.1002/lpor.202000062.

Broadband detection of multiple spin and orbital angular momenta via dielectric metasurface

Si Zhang[1,2], **Pengcheng Huo**[1,2], **Wenqi Zhu**[3,4], **Cheng Zhang**[5,6], **Peng Chen**[1,2], **Mingze Liu**[1,2], **Lu Chen**[3,4], **Henri J. Lezec**[3], **Amit Agrawal**[3,4], **Yanqing Lu**[1,2], **Ting Xu**[1,2]

[1]National Laboratory of Solid-State Microstructures, College of Engineering and Applied Sciences and Collaborative Innovation Center of Advanced Microstructures, Nanjing University, Nanjing, China

[2]Key Laboratory of Intelligent Optical Sensing and Manipulation, Ministry of Education, Nanjing University, Nanjing, China

[3]Physical Measurement Laboratory, National Institute of Standards and Technology, Gaithersburg, Maryland, United States

[4]Maryland NanoCenter, University of Maryland, College Park, Maryland, United States

[5]School of Optical and Electronic Information, Huazhong University of Science and Technology, Wuhan, China

[6]Wuhan National Laboratory for Optoelectronics, Huazhong University of Science and Technology, Wuhan, China

Abstract

Light beams carrying spin angular momentum (SAM) and orbital angular momentum (OAM) have created novel opportunities in the areas of optical communications, imaging, micromanipulation and quantum optics. However, complex optical setups are required to simultaneously manipulate, measure and analyze these states, which significantly limits system integration. Here, we introduce a novel detection approach for measuring multiple SAM and OAM modes simultaneously through a planar nanophotonic demultiplexer based on an all-dielectric metasurface. Coaxial light beams carrying multiple SAM and OAM states of light upon transmission through the demultiplexer are spatially separated into a range of vortex beams with different topological charge, each propagating along a specific wavevector. The broadband response, material dispersion and momentum conservation further enable the demultiplexer to achieve wavelength demultiplexing. We envision the ultracompact multifunctional architecture to enable simultaneous manipulation and measurement of polarization and spin encoded photon states with applications in integrated quantum optics and optical communications.

Author Contributions

S. Z., P. H., W. Z. and C. Z. contributed equally. All authors contributed to the interpretation of results and participated in manuscript preparation. T. X. directed the project.

Competing interests

The authors declare no competing financial interests.

Introduction

In the study of optics, a light beam is able to carry both spin and orbital angular momenta parallel to the wavevector direction (1). Spin angular momentum (SAM) is associated with the circular polarization state of light with each photon carrying SAM of $\pm h/2\pi$, where h is the Planck's constant and the sign denotes the handedness of light. One important application of SAM is the polarization division multiplexing (PDM) technique used in optical communications (2). On the other hand, a light beam carrying orbital angular momentum (OAM), also known as a vortex beam, exhibits a spiral phase front of $\exp(il\theta)$, where θ is the azimuthal angle and l is the topological charge (3). The spatial orthogonality between different OAM modes guarantees that each mode can be coded and transferred as an independent information channel, and theoretically large value of l can therefore provide enormous information capacity (4). Therefore, OAM has been considered as promising information carrier in optical and quantum communication systems (5–7). Combined with PDM and wavelength division multiplexing (WDM) techniques, OAM communication systems can support data capacities up to the terabits per second scale (8, 9).

Generally, OAM multiplexing communication usually involves information generation, transmission and demultiplexing. OAM generation can be achieved by using spiral phase plates (10, 11), *q*-plates (12–14), forked grating holograms (15, 16) or other nanophotonic methods (17, 18). The generated vortex beam can then transmit either in free-space or vortex fiber, and finally the OAM information is demultiplexed (19). OAM demultiplexing is typically realized using plasmonic devices (20–23), Dammann vortex gratings (24–26) or transformation optical systems (27–30). Undoubtedly, these methods provide new routes to detect the input OAM modes, however they introduce other imperfections such as large energy dissipation in plasmonic systems and the inevitable physical distance between the unwrapper and the phase corrector in transformation optical systems. In addition, as the generated OAM can inherit circular polarization state of incident light due to SAM-to-OAM conversion (31), physically separating SAM and OAM is also critically important during the demultiplexing process.

In this paper, based on an all-dielectric metasurface (32–38), we propose and demonstrate a single layer demultiplexer for multi-dimensional light field detection that includes simultaneous identification of the eigenstates and superposition states of SAM and OAM as well as the wavelength information. The metasurface demultiplexer utilizes two types of phase modulation approaches and exhibits high efficiency due to the low-loss characteristic of the constituent dielectric material. When coaxial light beams with different SAM and OAM states transmit through the demultiplexer, they are diffracted into a series of vortex beams propagating along specific wavevectors. The intrinsic spin and orbital angular momentum information of the light beam is then translated into a spatial intensity distribution, which can be conveniently collected and measured using a simple imaging system. Moreover, the broadband response, material dispersion and conservation of momentum enables the metasurface device to also demultiplex wavelength information. Therefore, the input light field consisting of a superposition of various SAM, OAM and wavelength states, can be demultiplexed and processed as individual spatially separated channels. We envision this work to inspire creation of an ultracompact flat-profile

nanophotonic device platform for efficient manipulation and detection of multiple spin and orbital angular momenta states, and further promote their applications in integrated optical and quantum communication systems.

Results

Principle of OAM and SAM Detection

Vortex beam carrying OAM is described by Laguerre-Gauss mode as $E_{\mathrm{OAM}} = E_0(r)e^{il\varphi}e^{i\boldsymbol{k}_0 \cdot \boldsymbol{x}}$, where r and φ are the radial and azimuthal coordinates, respectively, and exhibits a phase singularity at the center of beam intensity profile. In principle, a series of vortex beams can be generated using phase-only modulation metasurface with transmission function defined as $t(r) = \sum_n A_n(r)e^{il_n\varphi}e^{i\boldsymbol{k}_n \cdot \boldsymbol{x}}$, where $A_n(r)$ and $\boldsymbol{k}_n$ determines the intensity and wavevector of the nth beam carrying a topological charge l_n. Conversely, when a vortex beam carrying topological charge l_{in} is incident on the same metasurface, the output light field at the Fourier plane can be calculated by Fraunhofer diffraction as $E_{out} = \mathcal{F}[E_{OAM} \cdot t(r)]$. Considering a normal incidence vortex beam propagating along the z-axis (Fig. 1A), the diffracted field is written as:

$$E_{out} = \sum_n \left[E_{OAM}(r)e^{i(l_{in}+l_n)\varphi}e^{i\left(k_{xn}x + k_{yn}y\right)} \right] \tag{1}$$

where k_{xn} and k_{yn} determines the propagating direction of the nth output beam carrying topological charge $(l_{in} + l_n)$. Each vortex beam forms an independent, spatially separated information channel. At the channel where the modulated topological charge $l_{in} + l_n = 0$, the transmitted vortex beam degenerates to fundamental Gaussian mode with a vanishing singularity. Therefore, according to the intensity distribution of diffracted channel with a bright intensity spot at the center, it is possible to identify the input OAM mode.

To further increase the detection dimension, SAM demultiplexing can also be introduced to the aforementioned OAM detection procedure. To simultaneously transfer SAM and OAM information into the spatial intensity distribution, the transmission function of the metasurface is modified to

$$t_{\sigma_\pm}(r) = \sum_n A_{n,\sigma_\pm}(r)e^{il_{n,\sigma_\pm}\varphi}e^{i\left(k_{xn,\sigma_\pm}x + k_{yn,\sigma_\pm}y\right)} \tag{2}$$

where spin quantum number $\sigma_\pm = \pm 1$ represent the two orthogonal spin states $|\sigma_+\rangle = \begin{bmatrix} 1 \\ i \end{bmatrix}$ and $|\sigma_-\rangle = \begin{bmatrix} 1 \\ -i \end{bmatrix}$, denoting left-hand circular polarization (LCP) and right-hand circular polarization (RCP), respectively. The device is expected to generate different phase modulation for opposite handedness, and thus the information channel for the two circular polarization states would propagate along different directions. In addition, to increase the channel quantity from n to $2n$, the generated phase modulation for different OAM state is required to be decoupled from the SAM state. This is a difficult task in traditional device

using geometric phase or resonant phase, but achievable in a spin-multiplexing metasurface system, as described here.

Figure 1A shows the optical setup incorporating metasurface demultiplexer to simultaneously detect the OAM and SAM states. The phase distribution of the multifunctional metasurface is designed to be

$$\Phi_{\sigma_\pm}(x, y) = arg\ (e^{il_0\varphi}e^{\pm ik_x x} + \sum_n e^{il_n\varphi}e^{i(k_{xn}x \pm k_{yn}y)}) \quad (3)$$

where l_n takes nonzero integer values from −5 to +5. LCP and RCP channels with $l_n \neq 0$ are separated in far-field along the y-axis direction by controlling the phase distribution to provide opposite k_y values for the two circular polarization states, while channels with $l_0 = 0$ are separated along the x-axis with opposite k_x values. The calculated phase distribution $\Phi_{\sigma_+}(x, y)$ and $\Phi_{\sigma_-}(x, y)$ at the central 25 μm × 25 μm area of the metasurface are shown in Fig. 1B. As an illustration, for an incident vortex beam $|\sigma_+\rangle|+1\rangle$ generated from a q-plate, Fig. 1C plots the corresponding spiral phase front and donut-shape intensity distribution. When the vortex beam is normally incident on the metasurface demultiplexer, it will be modulated and diffracted into different channels propagating along specific beam direction (k_{xn}, k_{yn}), as shown in Fig. 1D. The diffraction pattern consists of beams with different topological charge and the corresponding ring radius r is proportional to $\sqrt{|l_{in} + l_n|}$. As the input field is pure LCP light, there are eleven channels existing in the y ≥ 0 coordinate area and the fundamental Gaussian mode profile appearing at the channel position where $l_n = -1$. Therefore, it is convenient to analyze the input SAM and OAM state information according to the position of the diffracted spots without a central singularity. Due to the orthogonality of OAM modes and SAM states, this approach is theoretically able to detect more complex superposition states of the incident light field.

Design of Metasurface Demultiplexer

The multifunctional metasurface described above requires uncorrelated phase modulation $\Phi_{\sigma_+}(x, y)$ and $\Phi_{\sigma_-}(x, y)$ for the incident LCP and RCP light beams, respectively. The metasurface satisfying such condition can be described by the Jones Matrix $J(x, y)$, where $J(x, y)|\sigma_+\rangle = e^{i\Phi_{\sigma_+}(x, y)}|\sigma_-\rangle$ and $J(x, y)|\sigma_-\rangle = e^{i\Phi_{\sigma_-}(x, y)}|\sigma_+\rangle$. When incident light with linear polarization interacts with the designed metasurface, the LCP component is modulated with phase factor $e^{i\Phi_{\sigma_+}(x, y)}$ and demultiplexed into channels appearing at $y \geq 0$ coordinate area, while the RCP component is modulated with phase factor $e^{i\Phi_{\sigma_-}(x, y)}$ and demultiplexed into $y \leq 0$ channels (Fig. 2A). The corresponding Jones Matrix is expressed as

$$J(x, y) = \frac{1}{2}\begin{bmatrix} e^{i\Phi_{\sigma_+}(x, y)} + e^{i\Phi_{\sigma_-}(x, y)} & ie^{i\Phi_{\sigma_-}(x, y)} - ie^{i\Phi_{\sigma_+}(x, y)} \\ ie^{i\Phi_{\sigma_-}(x, y)} - ie^{i\Phi_{\sigma_+}(x, y)} & -e^{i\Phi_{\sigma_+}(x, y)} - e^{i\Phi_{\sigma_-}(x, y)} \end{bmatrix} \quad (4)$$

On the basis of the eigenvalues and eigenvectors of $J(x, y)$, it is found that an anisotropic element with its optical axis rotated by a specific angle along the x-y plane can satisfy the

above conditions. The calculations show that the orientation angle θ is defined by function $\theta(x, y) = 1/4\left[\Phi_{\sigma_+}(x, y) - \Phi_{\sigma\_}(x, y)\right]$, and the phase shift parallel and perpendicular to the optical axis satisfy $\delta_x(x, y) = 1/2\left[\Phi_{\sigma_+}(x, y) - \Phi_{\sigma\_}(x, y)\right]$ and $\delta_y(x, y) = 1/2\left[\Phi_{\sigma_+}(x, y) - \Phi_{\sigma\_}(x, y)\right] - \pi$, respectively (detailed derivation shown in Supporting Information Section S1). The orientation angle is commonly known to control the geometric phase from 0 to 2π in nanopillars, while the phase shifts δ_x and δ_y are the waveguide phase accumulated upon propagation through the nanopillars. Using a set of nanopillars that can provide δ_x and δ_y covering the 0 to 2π phase range, it is feasible to design a functional device with arbitrary phase distribution $\Phi_{\sigma_+}(x, y)$ and $\Phi_{\sigma\_}(x, y)$.

In our experiment, the metasurface is composed of titanium dioxide (TiO_2) nanopillar arrays periodically arranged on a fused-silica substrate. TiO_2 is an outstanding candidate as the constituent material for the metasurface operating at visible frequencies because of its high refractive index and a relatively low absorption loss. Figure 2B depicts a single nanopillar structure unit cell, composed of a TiO_2 nanopillar (blue square) with a given height h = 600 nm arranged in a square lattice of pitch $P_x = P_y$ = 450 nm. The in-plane lateral dimensions of the nanopillar perpendicular and parallel to the optical axis are defined as L_x and L_y respectively, which are optimized to achieve the desired phase shifts δ_x and δ_y. The orientation angle θ distribution can be independently adjusted according to the calculation result of $1/4\left[\Phi_{\sigma_+} - \Phi_{\sigma\_}\right]$ to provide the required geometric phase. Independent control of (L_x, L_y) and θ distribution can therefore guarantee the decoupling of waveguide phase and geometric phase. To cover phase shifts δ_x and δ_y from 0 to 2π at a central wavelength of 530 nm, the continuous phase is approximated into eight discrete phase levels (Fig. 2C). Eight phase levels correspond to four basic units with structural parameters (L_x, L_y) and their mirror structures of dimension (L_y, L_x). As the polarization conversion efficiencies (detailed discussion shown in Supporting Information Section S2) of nanostructures dominate the modulation efficiency of the metasurface device, a set of four structural parameters (L_x, L_y) are optimized such that the nanopillars' polarization conversion efficiencies are relatively high across the entire visible range (Fig. 2D), which is also a prerequisite for efficient broadband operation of the metasurface device. The polarization conversion efficiencies are obtained by calculating the transmission coefficients and phase shifts for different structure parameters (Supplementary Fig. S1). An optical image of the fabricated metasurface device and a scanning electron micrograph (SEM) of the fabricated TiO_2 nanopillar array are shown in Fig. 2E and 2F respectively. The numerical simulation process and fabrication details are provided in the Methods section.

To demonstrate that the metasurface is capable of demultiplexing OAM modes across the entire visible range, a supercontinuum laser source attached to an acoustic optical tuning filter (AOTF) is used to generate light beams at three different wavelengths: λ_0 = 630 nm, 530 nm and 480 nm. The corresponding captured output diffraction patterns are shown in Fig. 2G – 2I. There are 22 channels designed for the OAM topological charges ranging from −5 to +5 with linear polarization state. At the position where coordinate y = 0, two channels are designed with an additional topological charge l_0 = 0 for the basic Gaussian mode, appearing at the left and right part of the screen for LCP and RCP incident light,

respectively. At the upper half of the screen, ten output channels are generated for LCP components, including five channels with smaller deflection angles carrying additional topological charge $l_n = -1, -2 \ldots -5$ from the left to right, and other five channels with larger deflection angles carrying $l_n = +5, +4 \ldots +1$. Each channel forms a donut-shape intensity profile on the screen with different ring radius each proportional to the value of $\sqrt{|l_n|}$. At the bottom half of the screen, the output channels for RCP components are symmetric to those of the LCP components, since the modulated deflecting phase satisfies $\varphi_{l_n,\sigma_+} = e^{i(k_{xn}x + k_{yn}y)}$ and $\varphi_{l_n,\sigma_-} = e^{i(k_{xn}x - k_{yn}y)}$.

In addition, chromatism is observed in the experiments, where output beams propagate along with different diffraction angles for different wavelengths. The measured output field intensity under simultaneous incidence of three wavelengths is shown in Fig. 2J, and the corresponding calculated result is shown in supplementary Fig. S2. This originates from the conservation of optical momentum and thus the deflection angle is positively correlated to the input wavelength. As a result, the device is capable of integrating OAM and SAM detection functionality together with the WDM capability.

Detection of spin and orbital angular momenta via metasurface demultiplexer

Experimental verification of simultaneous SAM and OAM detection by the metasurface device is shown in Fig. 3. A circularly polarized laser beam at a wavelength $\lambda_0 = 530$ nm, the same as the designed central wavelength, is incident on a liquid crystal *q*-plate to generate vortex beam with SAM and OAM states as $|\sigma_+\rangle|+1\rangle$ (Fig. 3A). The measured intensity profile and the corresponding calculated phase distribution are shown in Fig. 3A (*i*) and (*ii*), respectively. To calibrate the generated vortex beam, the measured intensity distribution of the interference field between the incident and the coaxial Gaussian beam via a Mach-Zehnder configuration are shown in Fig. 3A (*iii*), which is consistent with the theoretical predictions shown in Fig. 3A (*iv*). After calibration, the intensity distribution of the output field from the metasurface illuminated by the light beam carrying SAM and OAM information $|\sigma_+\rangle|+1\rangle$ is recorded on the screen (Fig. 3B). Consistent with the designed spin-dependent transmission function, the output channels for incident LCP light appear at the upper half ($y \geq 0$) area of screen, where the modulated deflecting phase items are given as $e^{i(k_{xn}x + k_{yn}y)}$ for $|\sigma_+\rangle$ state. As shown in Fig. 3B, for the channel with additional topological charge $l_n = -1$ marked by the white dashed circle, the diffract ion pattern is restored into the basic Gaussian mode with a bright center (Fig. 3C), while other channels still maintain the donut-shape intensity profile. Therefore, based on the position of the restored channel, the input SAM and OAM state can be inferred to be $|\sigma_+\rangle|+1\rangle$.

Similarly, the detection is also performed for input field $|\sigma_-\rangle|-4\rangle$, as shown in Fig. 3D to 3F. It can be seen that the measured beam profile in Fig. 3D (*i*) has the same donut-shape topology to that in Fig. 3A (*i*) but a different ring radius r_{in} due to $r_{in} \propto \sqrt{|l_{in}|}$. The calculated centrosymmetric phase distribution is shown in Fig. 3D (*ii*). Moreover, in Fig. 3D (*iii*) and (*iv*), the topological charge can be obtained from the number of petals, and as expected the rotation direction is opposite to that in Fig. 3A (*iii*) and (*iv*) because of opposite sign of the topological charge. After demultiplexing, Fig. 3E presents the output field intensity

distribution for $|\sigma_-\rangle|-4\rangle$. As the modulated phase is given as $e^{i(k_{xn}x - k_{yn}y)}$ for $|\sigma_-\rangle$ state, the output channels appear at the lower half ($y \leq 0$) of the screen. The magnified image of the channel with an additional topological charge $l_n = +4$ and a bright center spot is shown in Fig. 3F, which indicates that the input light information is $|\sigma_-\rangle|-4\rangle$. In addition, the calculated and measured detection results for a total of 10 × 2 combinations of SAM and OAM states are shown in supplementary Fig. S3 and S4, respectively.

Besides the simultaneous detection of arbitrary combination of SAM and OAM information using phase singularity, the metasurface is also capable of detecting cylindrical vector beams (CVBs), which is one typical form of the superposition states of SAM and OAM and can be deposed into two vortex beams with opposite spin states (39). CVB mode can be described by Jones Matrix $J_{CVB_m} = \frac{1}{\sqrt{2}}e^{-i(m\theta + \varphi_0)}|\sigma_+\rangle + \frac{1}{\sqrt{2}}e^{i(m\theta + \varphi_0)}|\sigma_-\rangle$, where m is the polarization topological charge and φ_0 is the initial polarization angle. Therefore, in this configuration, CVB mode can be demultiplexed into two information channels $|\sigma_+\rangle|-m\rangle$ and $|\sigma_-\rangle|+m\rangle$. The experimental demonstration is performed with incident CVBs carrying polarization topological charge $m_{in} = -3$, generated from a *q*-plate illuminated by a linearly polarized light. The measured and calculated donut-shaped intensity profiles of the input light are shown in Fig. 3G (*i*) and (*ii*), respectively, and the red arrows in (*ii*) represent the calculated polarization distribution exhibiting a polarization singularity at the center. Utilizing a linear polarizer, the measured and calculated polarized intensity distributions are shown in Fig. 3G (*iii*) and (*iv*), which has a flower-shaped profile with $|2m|$ petals. The corresponding detection result by the metasurface is given in Fig. 3H, where the measured output beams are restored into basic Gaussian modes only at the position of channels $|\sigma_+\rangle|+3\rangle$ and $|\sigma_-\rangle|-3\rangle$, indicating $m_{in} = -3$. The magnified images of the restored channels are shown in Fig. 3I. Therefore, the metasurface device can be easily used to detect CVB modes directly without any complex optical setup. The calculated and measured output field intensity distributions for vector beams carrying polarization topological charge m from −5 to +5 are shown in supplementary Fig. S5 and S6, respectively.

Beyond the SAM and OAM responses, incorporation with the WDM technique can further increase the dimension of the detected information. Based on the experimental setup shown in supplementary Fig. S7, the simultaneous detection of SAM, OAM and wavelength information for a complex input light field is presented in Fig. 4. Two light beams with wavelengths $\lambda_1 = 630$ nm and $\lambda_2 = 530$ nm are given arbitrary SAM and OAM information and coaxially incident on the metasurface through a beam splitter. Figure 4A (*i*) and (*ii*) respectively show the measured and calculated intensity profiles of the first complex incident light field at the wavelength of $\lambda_1 = 630$ nm described by Jones Matrix $|\lambda_1\rangle = \frac{1}{\sqrt{2}}|\sigma_+\rangle|+3\rangle + \frac{1}{\sqrt{2}}|\sigma_-\rangle|0\rangle$, in which the white ellipses denote the calculated polarization distribution. It is observed that the incident pattern rotates with the angle of the polarizer changing from 0° (Fig 4A (*iii*)) to 90° (Fig. 4A (*iv*)) along the *x*-axis. The second complex input field at wavelength of $\lambda_2 = 530$ nm is the superposition of vortex beams carrying OAM $|+2\rangle$ and $|-2\rangle$ with linear polarization, and the measured and calculated intensity distributions are shown in Fig. 4B (*i*) and (*ii*), respectively. According to the Malus Law, the measured intensity of $|\lambda_2\rangle$ reaches maximum and minimum with the polarization angle of

polarizer at 0° (Fig. 4B (*iii*)) and 90° (Fig. 4B (*iv*)), respectively. The measured and calculated intensity distributions of output fields upon simultaneous illumination of the metasurface with superposition fields $|\lambda_1\rangle + |\lambda_2\rangle$ are shown in Fig. 4C and 4D, respectively. As expected, it turns out that the complex input fields can be demultiplexed into six spatially separable channels with bright center spots (R_1, R_2, G_1, G_2, G_3 and G_4), which respectively correspond to $|\sigma_+\rangle|+3\rangle$, $|\sigma_-\rangle|0\rangle$, $|\sigma_+\rangle|+2\rangle$, $|\sigma_+\rangle|-2\rangle$, $|\sigma_-\rangle|+2\rangle$ and $|\sigma_-\rangle|-2\rangle$ states. The magnified images of these six channels in the experiment and calculations are shown in Fig. 4E and 4F, respectively. These results demonstrate that SAM, OAM and wavelength demultiplexing and detection can be integrated into a single layer metasurface without the need for complex optical setups. Additional calculations and measurements of the detection for incident light beams with same SAM and OAM states but different wavelengths are given in supplementary Fig. S8. It should be emphasized that the difference of wavelengths should be large enough to prevent spatial crosstalk. Moreover, to provide enough separation distance of the same channel for different wavelengths, the deflection angle can be further increased by design but must be within the acceptance numerical aperture of the imaging system.

Discussion

In summary, we theoretically and experimentally demonstrate a phase-only modulation device that can achieve simultaneous detection of SAM, OAM and wavelength information based on a single-layer all-dielectric metasurface. Each fundamental optical mode, as a combination of specific SAM, OAM and wavelength information, is processed as an independent channel and demultiplexed into diffracted beams with different deflection angle. The device builds a unique connection between the intrinsic spin and orbital angular momenta, the wavelength of light and the spatial intensity distribution, which could be used to further increase the information channel capacity. Combined with advantages of planar architecture and ultrathin thickness, we envision to device to enable novel applications in integrated optical and quantum communication systems.

Materials and Methods

Numerical simulations

Metasurface demultiplexer was realized by deposing TiO_2 nanopillars on fused-silica substrate. The generated modulating phase is correlated with the structural parameters of nanopillar. To investigate the optimum parameters for providing phase modulation as designed, periodical nanopillar arrays with specific geometric parameters combination were simulated using finite-difference time-domain (FDTD) method. Nanopillars were arranged in square lattice with a lattice constant of 450 nm and fixed height of 600 nm. The used refractive indices of TiO_2 in the visible wavelength range were obtained from ellipsometry measurements of TiO_2 thin film. The boundary conditions were set as periodical conditions at the directions in-plane to simulate the periodical nanopillar arrays. And in the situation of transmitting, the boundary conditions were set as perfect match layers in the direction of light incidence. Planer monochromatic light source with wavelength of 530 nm was used to

extract the transmission coefficients and phase shifts along *x*- and *y*-axis with the lateral and vertical lengths of nanopillars as shown in Fig. S1.

Metasurface fabrication

First, fused silica substrates with thickness of 500 μm thick were prime-vapor-coated with a monolayer of hexamethyl disilazane (HMDS) and then spin-coated with a layer of 600 nm thick, ZEP520A positive-tone electron beam (e-beam) resist (40). Next, the samples were coated with a layer of 10 nm thick aluminum (Al) via thermal evaporation, which suppressed any charging effects during the subsequent e-beam lithography step. The e-beam lithography was performed at an accelerating voltage of 100 kV and a beam current of 2 nA. The samples were developed in hexyl-acetate for 120 s. Next, the patterned samples were coated with TiO_2 using atomic layer deposition (ALD). The ALD was done at a low temperature of 90 °C to avoid deformation of the resist pattern. After the ALD, the overcoated TiO_2 layer was etched by inductively coupled plasma reactive ion etching (ICP-RIE), with a gas mixture of Cl_2 and BCl_3. The etching was stopped when the overcoated TiO_2 had been fully removed and the e-beam resist was exposed. Finally, the samples were exposed to UV irradiation, followed by soaking in n-methyl-2-pyrrolidone, which removed the resist and produced the array of TiO_2 nanopillars with predesigned geometries.

Supplementary Material

Refer to Web version on PubMed Central for supplementary material.

Acknowledgement

The work is supported by the Key Research and Development Program from Ministry of Science and Technology of China (2016YFA0202100 and 2017YFA0303700) and National Natural Science Foundation of China (11774163). W. Z., L. C. and A. A. acknowledge support under the Cooperative Research Agreement between the University of Maryland and the National Institute of Standards and Technology, Award#70-NANB14H209, through the University of Maryland.

References

1. Allen L, Beijersbergen MW, Spreeuw R, Woerdman J, Orbital angular momentum of light and the transformation of Laguerre-Gaussian laser modes. Phys. Rev. A 45, 8185 (1992). [PubMed: 9906912]
2. Wang J, He S, Dai D, On-chip silicon 8-channel hybrid (de)multiplexer enabling simultaneous mode- and polarization-division-multiplexing. Laser Photonics Rev. 8, L18–L22 (2014).
3. Padgett M, Courtial J, Allen L, Light's orbital angular momentum. Phys. Today 57, 35–40 (2004).
4. Yao AM, Padgett MJ, Orbital angular momentum: origins, behavior and applications. Adv. Opt. Photonics 3, 161–204 (2011).
5. Gibson G, Courtial J, Padgett MJ, Vasnetsov M, Pas'ko V, Barnett SM, Franke-Arnold S, Free-space information transfer using light beams carrying orbital angular momentum. Opt. Express 12, 5448–5456 (2004). [PubMed: 19484105]
6. Wang J, Yang J-Y, Fazal IM, Ahmed N, Yan Y, Huang H, Ren Y, Yue Y, Dolinar S, Tur M, Terabit free-space data transmission employing orbital angular momentum multiplexing. Nat. Photonics 6, 488–496 (2012).
7. Yan Y, Xie G, Lavery MPJ, Huang H, Ahmed N, Bao C, Ren Y, Cao Y, Li L, Zhao Z, Molisch AF, Tur M, Padgett MJ, Willner AE, High-capacity millimetre-wave communications with orbital angular momentum multiplexing. Nat. Commun 5, 4876 (2014). [PubMed: 25224763]

8. Bozinovic N, Yue Y, Ren Y, Tur M, Kristensen P, Huang H, Willner AE, Ramachandran S, Terabit-Scale Orbital Angular Momentum Mode Division Multiplexing in Fibers. Science 340, 1545–1548 (2013). [PubMed: 23812709]
9. Huang H, Xie G, Yan Y, Ahmed N, Ren Y, Yue Y, Rogawski D, Willner MJ, Erkmen BI, Birnbaum KM, Dolinar SJ, Lavery MPJ, Padgett MJ, Tur M, Willner AE, 100 Tbit/s free-space data link enabled by three-dimensional multiplexing of orbital angular momentum, polarization, and wavelength. Opt. Lett 39, 197–200 (2014). [PubMed: 24562105]
10. Turnbull G, Robertson D, Smith G, Allen L, Padgett M, The generation of free-space Laguerre-Gaussian modes at millimetre-wave frequencies by use of a spiral phase plate. Opt. Commun 127, 183–188 (1996).
11. Ruffato G, Massari M, Romanato F, Generation of high-order Laguerre–Gaussian modes by means of spiral phase plates. Opt. Lett 39, 5094–5097 (2014). [PubMed: 25166082]
12. Piccirillo B, D'Ambrosio V, Slussarenko S, Marrucci L, Santamato E, Photon spin-to-orbital angular momentum conversion via an electrically tunable q-plate. Appl. Phys. Lett 97, 241104 (2010).
13. Slussarenko S, Murauski A, Du T, Chigrinov V, Marrucci L, Santamato E, Tunable liquid crystal q-plates with arbitrary topological charge. Opt. Express 19, 4085–4090 (2011). [PubMed: 21369237]
14. Milione G, Lavery MP, Huang H, Ren Y, Xie G, Nguyen TA, Karimi E, Marrucci L, Nolan DA, Alfano RR, 4 × 20 Gbit/s mode division multiplexing over free space using vector modes and a q-plate mode (de)multiplexer. Opt. Lett 40, 1980–1983 (2015). [PubMed: 25927763]
15. Granata M, Buy C, Ward R, Barsuglia M, Higher-order Laguerre-Gauss mode generation and interferometry for gravitational wave detectors. Phys. Rev. Lett 105, 231102 (2010). [PubMed: 21231445]
16. Shumei C, Yuan C, Guixin L, Shuang Z, Wai CK, Geometric metasurface fork gratings for vortex-beam generation and manipulation. Laser Photonics Rev. 10, 322–326 (2016).
17. Cai X, Wang J, Strain MJ, Johnson-Morris B, Zhu J, Sorel M, O'Brien JL, Thompson MG, Yu S, Integrated Compact Optical Vortex Beam Emitters. Science 338, 363–366 (2012). [PubMed: 23087243]
18. Miao P, Zhang Z, Sun J, Walasik W, Longhi S, Litchinitser NM, Feng L, Orbital angular momentum microlaser. Science 353, 464–467 (2016). [PubMed: 27471299]
19. Brunet C, Vaity P, Messaddeq Y, LaRochelle S, Rusch LA, Design, fabrication and validation of an OAM fiber supporting 36 states. Opt. Express 22, 26117–26127 (2014). [PubMed: 25401644]
20. Ren H, Li X, Zhang Q, Gu M, On-chip noninterference angular momentum multiplexing of broadband light. Science 352, 805–809 (2016). [PubMed: 27056843]
21. Li Y, Li X, Chen L, Pu M, Jin J, Hong M, Luo X, Orbital Angular Momentum Multiplexing and Demultiplexing by a Single Metasurface. Adv. Opt. Mater 5, 1600502 (2017).
22. Yue F, Wen D, Zhang C, Gerardot BD, Wang W, Zhang S, Chen X, Multichannel Polarization-Controllable Superpositions of Orbital Angular Momentum States. Adv. Mater 29, 1603838 (2017).
23. Hachtel JA, Cho S-Y, Davidson RB, Feldman MA, Chisholm MF, Haglund RF, Idrobo JC, Pantelides ST, Lawrie BJ, Spatially and spectrally resolved orbital angular momentum interactions in plasmonic vortex generators. Light: Sci. Appl 8, 33 (2019). [PubMed: 30911382]
24. Lei T, Zhang M, Li Y, Jia P, Liu GN, Xu X, Li Z, Min C, Lin J, Yu C, Niu H, Yuan X, Massive individual orbital angular momentum channels for multiplexing enabled by Dammann gratings. Light: Sci. Appl 4, e257 (2015).
25. Min C, Liu J, Lei T, Si G, Xie Z, Lin J, Du L, Yuan X, Plasmonic nano-slits assisted polarization selective detour phase meta-hologram. Laser Photonics Rev. 10, 978–985 (2016).
26. Chen P, Ma LL, Duan W, Chen J, Ge SJ, Zhu ZH, Tang MJ, Xu R, Gao W, Li T, Digitalizing self-assembled chiral superstructures for optical vortex processing. Adv. Mater 30, 1705865 (2018).
27. Berkhout GCG, Lavery MPJ, Courtial J, Beijersbergen MW, Padgett MJ, Efficient Sorting of Orbital Angular Momentum States of Light. Phys. Rev. Lett 105, 153601 (2010). [PubMed: 21230900]
28. Mirhosseini M, Malik M, Shi Z, Boyd RW, Efficient separation of the orbital angular momentum eigenstates of light. Nat. Commun 4, 2781 (2013). [PubMed: 24216691]

29. Malik M, Mirhosseini M, Lavery MPJ, Leach J, Padgett MJ, Boyd RW, Direct measurement of a 27-dimensional orbital-angular-momentum state vector. Nat. Commun 5, 3115 (2014). [PubMed: 24445503]
30. Wen Y, Chremmos I, Chen Y, Zhu J, Zhang Y, Yu S, Spiral transformation for high-resolution and efficient sorting of optical vortex modes. Phys. Rev. Lett 120, 193904 (2018). [PubMed: 29799240]
31. Devlin RC, Ambrosio A, Rubin NA, Mueller JPB, Capasso F, Arbitrary spin-to–orbital angular momentum conversion of light. Science 358, 896–901 (2017). [PubMed: 29097490]
32. Lin D, Fan P, Hasman E, Brongersma ML, Dielectric gradient metasurface optical elements. Science 345, 298–302 (2014). [PubMed: 25035488]
33. Arbabi A, Horie Y, Bagheri M, Faraon A, Dielectric metasurfaces for complete control of phase and polarization with subwavelength spatial resolution and high transmission. Nat. Nanotechnol 10, 937–943 (2015). [PubMed: 26322944]
34. Khorasaninejad M, Chen WT, Devlin RC, Oh J, Zhu AY, Capasso F, Metalenses at visible wavelengths: Diffraction-limited focusing and subwavelength resolution imaging. Science 352, 1190–1194 (2016). [PubMed: 27257251]
35. Kruk S, Kivshar Y, Functional Meta-Optics and Nanophotonics Governed by Mie Resonances. ACS Photonics 4, 2638–2649 (2017).
36. Tittl A, Leitis A, Liu M, Yesilkoy F, Choi D-Y, Neshev DN, Kivshar YS, Altug H, Imaging-based molecular barcoding with pixelated dielectric metasurfaces. Science 360, 1105–1109 (2018). [PubMed: 29880685]
37. Lin RJ, Su V-C, Wang S, Chen MK, Chung TL, Chen YH, Kuo HY, Chen J-W, Chen J, Huang Y-T, Wang J-H, Chu CH, Wu PC, Li T, Wang Z, Zhu S, Tsai DP, Achromatic metalens array for full-colour light-field imaging. Nat. Nanotechnol 14, 227–231 (2019). [PubMed: 30664753]
38. Fan QB, Zhu W, Liang Y, Huo P, Zhang C, Agrawal A, Huang K, Luo X, Lu YQ, Qiu CW, Lezec HJ, Xu T, Broadband generation of photonic spin-controlled arbitrary accelerating light beams in the visible. Nano Lett. 19, 1158–1165 (2019). [PubMed: 30595022]
39. Zhan Q, Cylindrical vector beams: from mathematical concepts to applications. Adv. Opt. Photonics 1, 1–57 (2009).

40. Certain commercial equipment, instruments, or materials are identified in this paper to foster understanding. Such identification does not imply recommendation or endorsement by the National Institute of Standards and Technology, nor does it imply that the materials or equipment identified are necessarily the best available for the purpose.

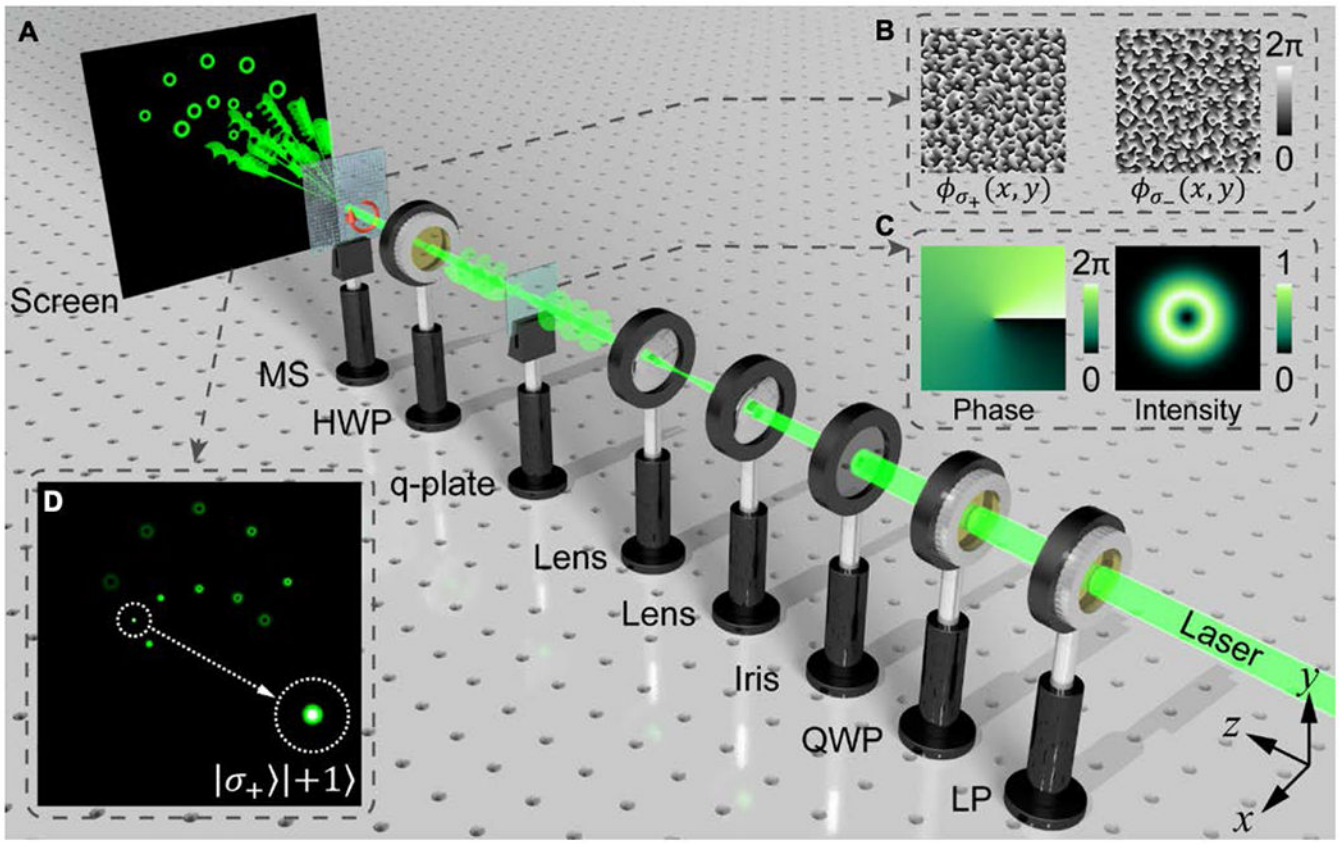

Figure 1. Schematic illustration of the experimental setup for optical spin and angular momentum detection.

(A) The green helicoids and red arrow indicate phase fronts and polarization state respectively. Optical elements: LP (linear polarizer), QWP (quarter-wave plate), HWP (half-wave plate) and MS (metasurface). (B) Designed phase distribution for LCP (left inset) and RCP (right inset) light from 0 to 2π in the central area of the functional metasurface used for demultiplexing. (C) Calculated phase (left inset) and normalized intensity (right inset) distribution of incident vortex beam generated by the q-plate. (D) Calculated intensity distribution on screen when incident with a vortex beam of spin and angular momentum state $|\sigma_+\rangle|+1\rangle$.

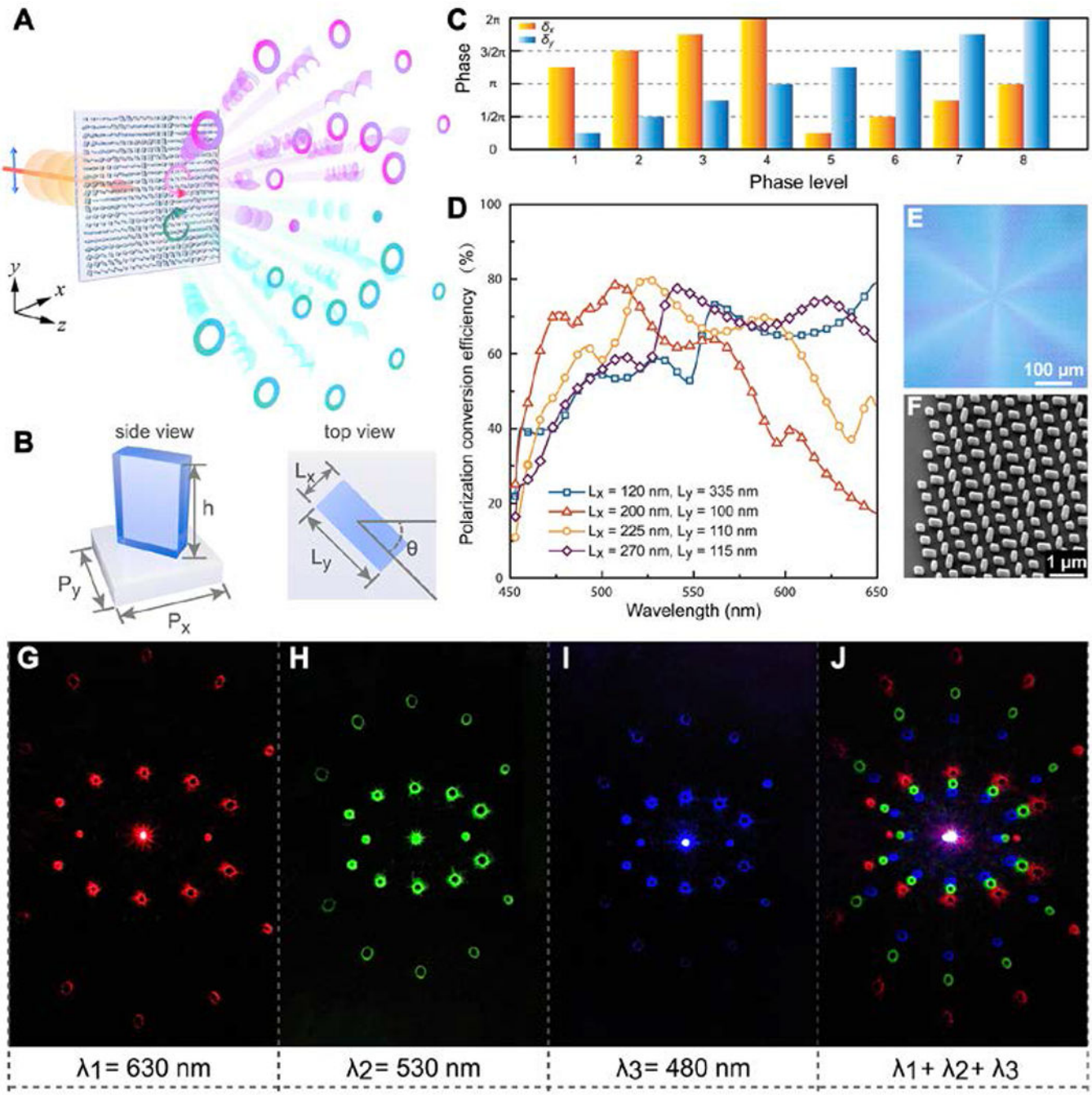

Figure 2. Metasurface demultiplexer formed by TiO_2 nanopillar array

(A) Schematic illustration of the vortex beam arrays with topological charge l_n from −5 to +5 separated by the metasurface demultiplexer. Blue arrow indicates linearly polarized incident plane wave. Magenta (cyan) helicoids and circles denotes the wavefronts and intensity profiles of left (right) circularly polarized components. Light carrying different spin angular momentum is spatially separated given opposite $\boldsymbol{k}_y$. (B) A typical unit cell of the functional metasurface with period P_x, P_y and height h (side view), as well as varying width L_x, length L_y and rotation angle θ along the x-y plane (top view). (C) Required phase shifts

δ_x and δ_y of eight phase levels to cover the phase distribution and correspond to eight different half-wave plate designs. (D) Calculated polarization conversion efficiency of four selected unit structures in the wavelength range from 450 nm to 650 nm. (E) Optical image of the metasurface device. (F) Scanning electron micrographs (SEMs) of fabricated structures captured from side view. Measured intensity distributions of the output field through metasurface demultiplexer at wavelength of (G) 630 nm, (H) 530 nm, (I) 480 nm. (J) Measured intensity distribution of the output field for three wavelengths illumination.

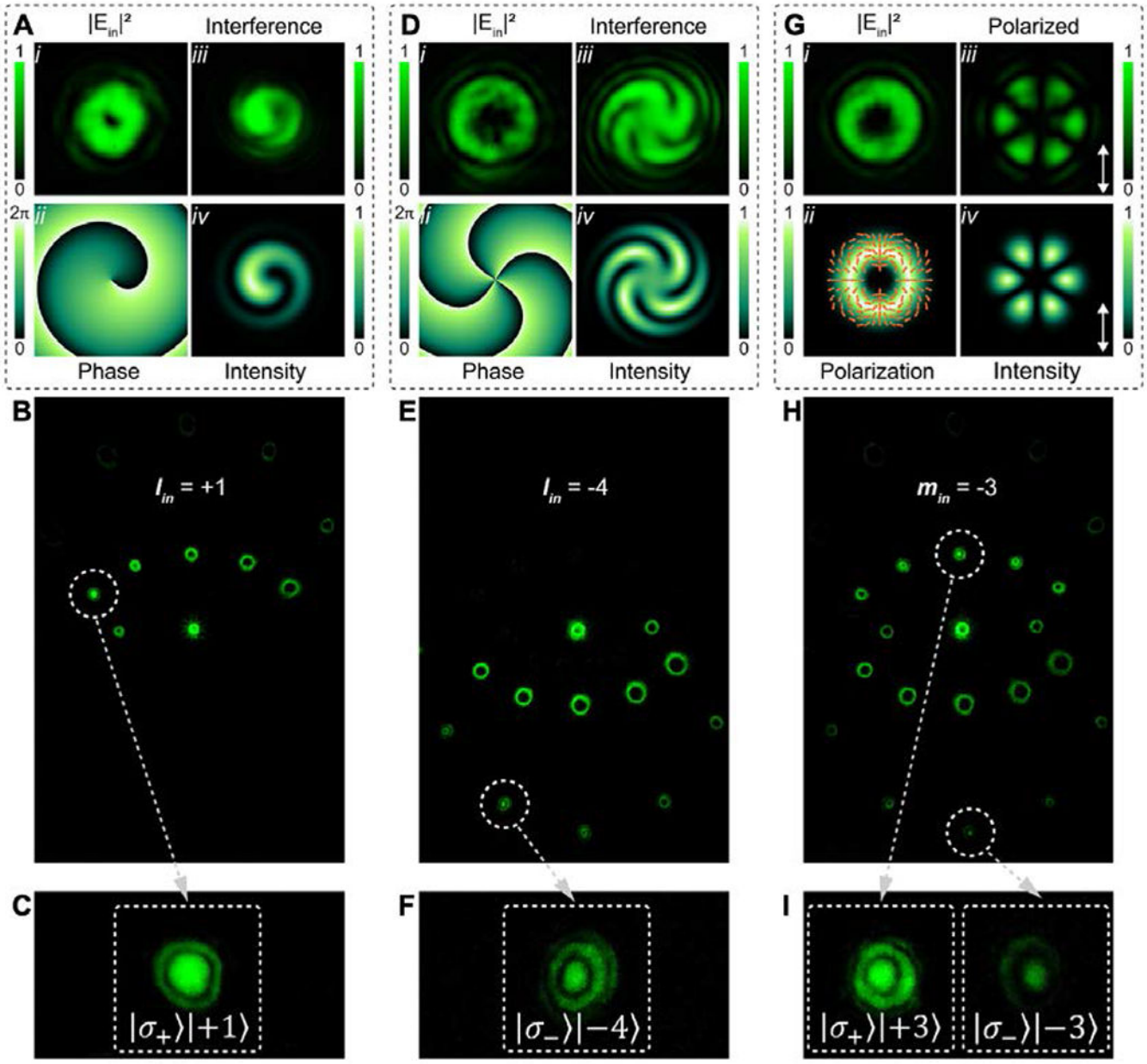

Figure 3. SAM and OAM detection by metasurface demultiplexer

(A) Incident vortex beam with topological charge l_{in} = +1. Inset: (*i*) Measured input intensity distribution. (*ii*) Calculated input phase distribution. Measured (*iii*) and calculated (*iv*) interference intensity distribution. (B) Measured output intensity distribution for the channel representing $|\sigma_+\rangle|+1\rangle$. (C) Magnification of corresponding channel with bright center. (D) Incident vortex beam with topological charge l_{in} = −4. Inset: (*i*) Measured input intensity distribution. (*ii*) Calculated input phase distribution. Measured (*iii*) and calculated (*iv*) interference intensity distribution. (E) Measured output intensity distribution for the channel representing $|\sigma_-\rangle|-4\rangle$. (F) Magnification of corresponding channel with bright center. (G) Incident vortex beam with polarization topological charge m_{in} = −3. Inset: (*i*) Measured input intensity distribution. (*ii*) Calculated input polarization distribution. Measured (*iii*) and

calculated (*iv*) intensity distribution after linear polarizer. (H) Measured output intensity distribution for channels representing $|\sigma_+\rangle|+3\rangle$ and $|\sigma_-\rangle|-3\rangle$. (I) Magnification of corresponding channel with bright center.

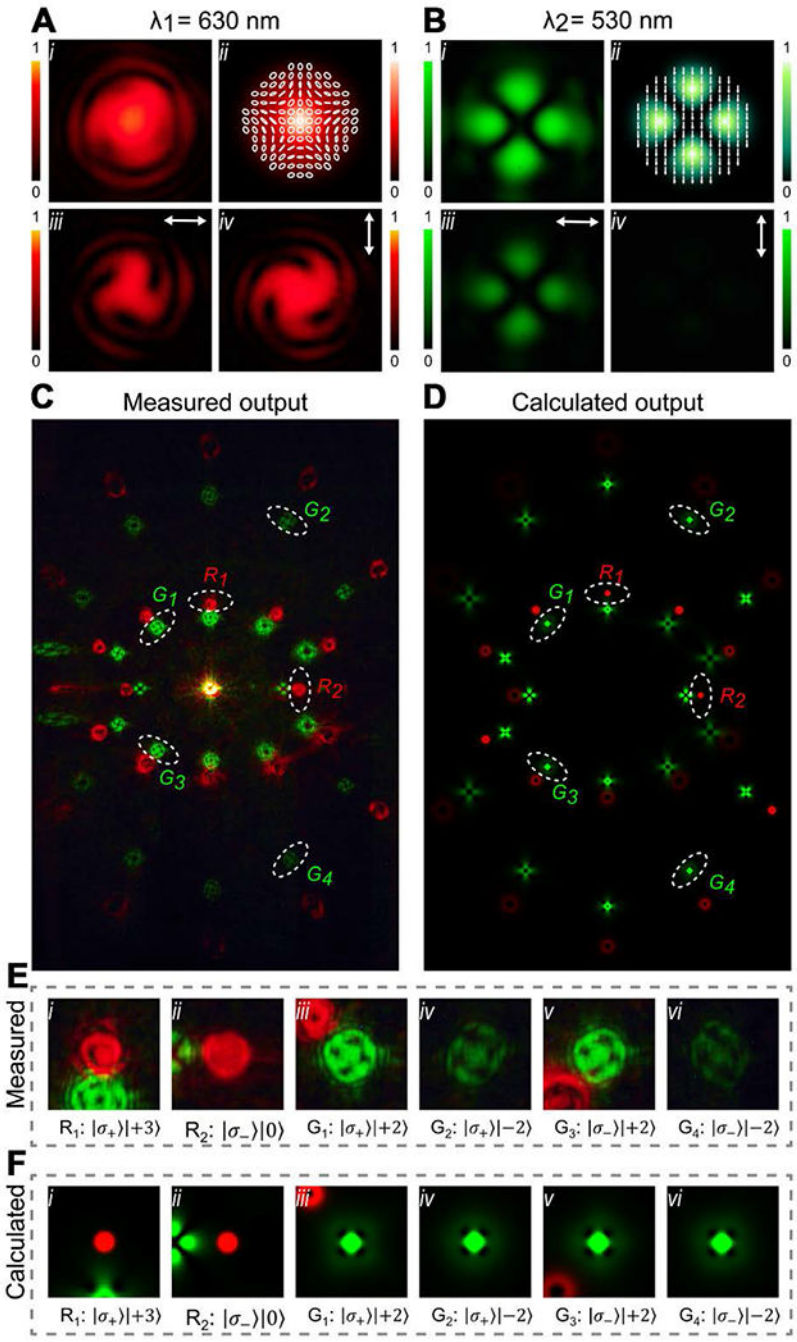

Figure 4. Metasurface demultiplexing complex light fields.

Incident optical fields as superposition of (A) vector vortex beam $|\lambda_1\rangle = 1/\sqrt{2}|\sigma_+\rangle|+3\rangle + 1/\sqrt{2}|\sigma_-\rangle|0$ and (B) vortex beam $|\lambda_2\rangle = 1/\sqrt{2}|+2\rangle + 1/\sqrt{2}|-2\rangle$. Inset: (*i*) measured intensity profile, (*ii*) calculated intensity profile and polarization distribution, and measured intensity profile after linear polarizer aligned at angle 0° (*iii*) and 90° (*iv*). (C) Measured and (D) calculated output intensity distributions after demultiplexing into six channels (*i*) R_1: $|\sigma_+\rangle|+3\rangle$, (*ii*) R_2: $|\sigma_-\rangle|0\rangle$, (*iii*) G_1: $|\sigma_+\rangle|+2\rangle$, (*iv*) G_2: $|\sigma_+\rangle|-2\rangle$, (*v*) G_3: $|\sigma_-\rangle|$

$+2\rangle$ and (*vi*) G_4: $|\sigma_-\rangle|-2\rangle$. Magnification of the corresponding channels with bright center for (E) experiment and (F) calculation results.